

SCIENTIFIC REPORTS

OPEN

Tuning Coupling Behavior of Stacked Heterostructures Based on MoS₂, WS₂, and WSe₂

Fang Wang, Junyong Wang, Shuang Guo, Jinzhong Zhang, Zhigao Hu & Junhao Chu

Received: 11 November 2016

Accepted: 13 February 2017

Published: 17 March 2017

The interlayer interaction of vertically stacked heterojunctions is very sensitive to the interlayer spacing, which will affect the coupling between the monolayers and allow band structure modulation. Here, with the aid of density functional theory (DFT) calculations, an interesting phenomenon is found that MoS₂-WS₂, MoS₂-WSe₂, and WS₂-WSe₂ heterostructures turn into direct-gap semiconductors from indirect-gap semiconductors with increasing the interlayer space. Moreover, the electronic structure changing process with interlayer spacing of MoS₂-WS₂, MoS₂-WSe₂, and WS₂-WSe₂ is different from each other. With the help of variable-temperature spectral experiment, different electronic transition properties of MoS₂-WS₂, MoS₂-WSe₂, and WS₂-WSe₂ have been demonstrated. The transition transformation from indirect to direct can be only observed in the MoS₂-WS₂ heterostructure, as the valence band maximum (VBM) at the Γ point in the MoS₂-WSe₂ and WS₂-WSe₂ heterostructure is less sensitive to the interlayer spacing than those from the MoS₂-WS₂ heterostructure. The present work highlights the significance of the temperature tuning in interlayer coupling and advance the research of MoS₂-WS₂, MoS₂-WSe₂, and WS₂-WSe₂ based device applications.

Semiconductor heterojunctions have played a significant role in the rich collection of unimagined electronic structures and optical properties¹. The emergence of atom-thin transition-metal dichalcogenides (TMDs) as a new class of two dimensional semiconducting materials, which are almost as thin, transparent, and flexible as graphene with a wealth of new physical phenomena²⁻⁵, creates exciting new opportunities to push semiconductor heterostructures toward a new frontier^{6,7}. Vertically stacked van der Waals TMDs heterostructures have been recognized as a powerful platform to create atomically thin heterostructures⁸⁻¹⁰. These heterojunctions have an optically active band gap with bound electrons and holes localized in individual monolayers^{11,12}, and their energy and luminescence intensity are highly tunable with the applied vertical gate voltage, laser intensity, and annealing time^{12,13}. A more desirable way to control the interlayer coupling properties is adjusting the interlayer spacing, which is closely related with the temperature^{14,15}. Temperature induces lattice parameter changes and modulates the band structure, altering the optical properties of the heterojunctions. Further more, it is important to investigate the temperature induced phenomena in order to distinguish the phenomena influenced by other factors, such as the surface quality, the strain applied on the heterostructures, and even the number of atomic layers, etc. However, such an interesting and important research of variable-temperature tuning for TMDs heterostructures has not been reported up to now.

In this article, high-quality MoS₂-WS₂, MoS₂-WSe₂, and WS₂-WSe₂ heterostructures have been fabricated by the polystyrene film transferred technique. They are systematically studied by tuning interlayer coupling with temperature for the first time. Furthermore, it is discovered that the temperature is an extremely sensitive factor to the interlayer coupling in comparison with the annealing tuning. Based on the density functional theory (DFT) calculations, an interesting phenomenon is found that MoS₂-WS₂, MoS₂-WSe₂, and WS₂-WSe₂ heterostructures turn into direct-gap semiconductors from indirect-gap semiconductors with increasing the interlayer space. However, in the MoS₂-WS₂, MoS₂-WSe₂, and WS₂-WSe₂ heterostructures, the change of the bandgap properties with interlayer spacing differs from each other. The results has been observed in the variable-temperature experiment. Our results not only compare the MoS₂-WS₂, MoS₂-WSe₂, and WS₂-WSe₂ heterostructures tuning character, but also open up a new direction for 2D applications where external modulation of bandgap and optical properties is desired.

Technical Center for Multifunctional Magneto-Optical Spectroscopy (ECNU), Shanghai Department of Electronic Engineering, East China Normal University, Shanghai 200241, China. Correspondence and requests for materials should be addressed to Z.H. (email: zghu@ee.ecnu.edu.cn)

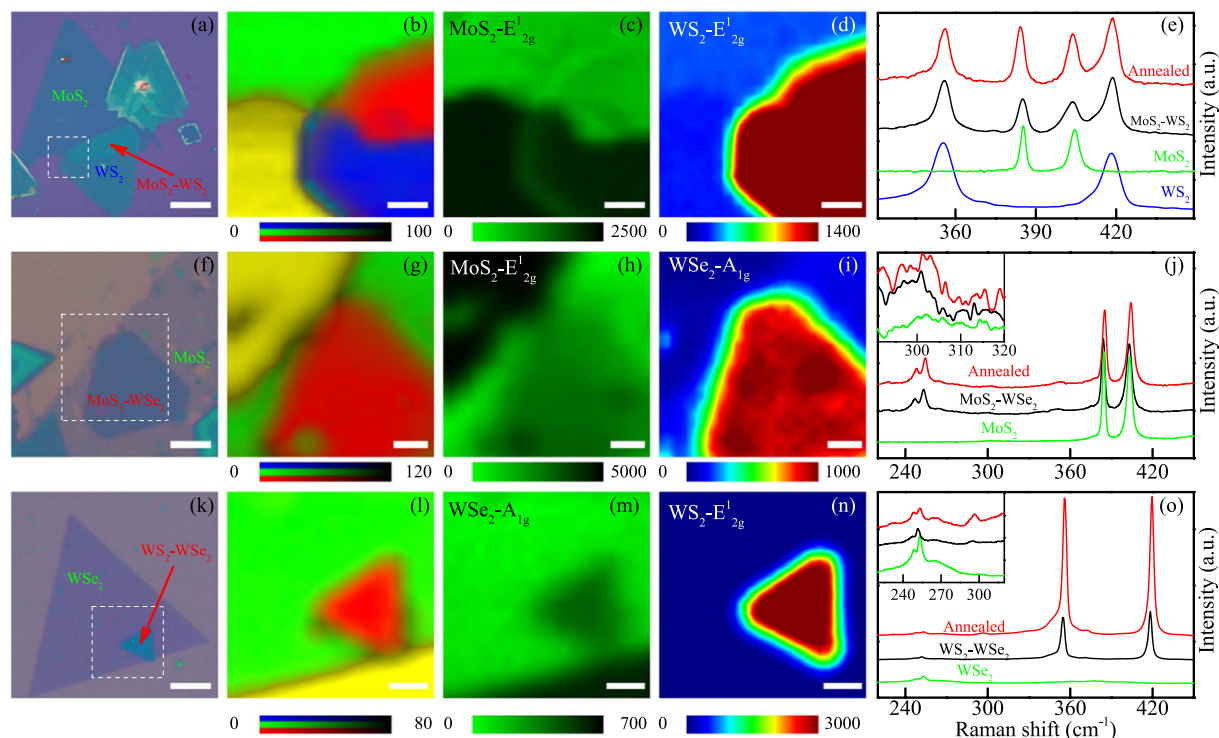


Figure 1. TMDs heterostructures prepared by the PS film transfer technique. (a,f,k) Optical microscope image of MoS₂-WS₂, MoS₂-WSe₂, and WS₂-WSe₂ heterostructures. (b,g,l) Raman mapping in the confocal measurements for the heterostructures in the dashed frame region in panels (a), (f), and (k). The yellow parts correspond to the substrates, the green, blue parts refer to the single TMDs regions, and red parts refer to heterogeneous regions. (c,h,m) Single color mapping of Raman intensity at the 385 cm⁻¹ (E_{2g}¹ mode in MoS₂) and 356 cm⁻¹ (A_{1g} mode in WSe₂). (d,i,n) Pseudo-color mapping of Raman intensity at 356 cm⁻¹ (E_{2g}¹ mode in WS₂) and 254 cm⁻¹ (A_{1g} mode in WSe₂). (e,j,o) The Raman spectra of the MoS₂-WS₂, MoS₂-WSe₂, and WS₂-WSe₂ heterostructures corresponding to the different region in panels (b), (g), and (l). Scale bars of panels (a), (f), and (k) are 20 μm, 4 μm, and 6 μm, respectively. Scale bar of panels (b-d) are 4 μm; that of panels (g-i) and (l-n) are 2 μm. The colour scale bars in the bottom of (b-d), (g-i), and (l-n) correspond to the intensity of the Raman spectra.

Results and discussion

Raman scattering. The vertically stacked heterostructures have been investigated by Raman scattering and PL spectroscopy. The optical images and Raman spectra are shown in Fig. 1. It indicates that the MoS₂-WS₂, MoS₂-WSe₂, and WS₂-WSe₂ heterostructures have been stacked successfully. The monolayer and heterostructure regions can be readily distinguished under the optical microscope and Raman mapping.

The E_{2g}¹ and A_{1g} Raman modes are located at 385.1 cm⁻¹ and 404.4 cm⁻¹ for monolayer MoS₂ [green line in Fig. 1(e)], whereas those for monolayer WS₂ are 356.1 cm⁻¹ and 417.4 cm⁻¹ [blue line in Fig. 1(e)]¹⁶⁻¹⁸. The Raman spectra recorded on the MoS₂-WS₂ heterostructure [black line in Fig. 1(e)] seem to be a simple superposition of the monolayer MoS₂ and WS₂. Even after the annealing at 100 °C in argon gas for 6 hours, except for increasing the intensity [red line in Fig. 1(e)]¹³. The frequency difference between the E_{2g}¹ and A_{1g} Raman modes is 18.6 cm⁻¹ for monolayer MoS₂ in MoS₂-WSe₂ [green line in Fig. 1(j)], and 4.7 cm⁻¹ for monolayer WSe₂ in WS₂-WSe₂ [green line in Fig. 1(o)], respectively¹⁹. While in the WSe₂-based heterostructures, an additional weak Raman peak pointed to interlayer coupling near 300 cm⁻¹ can be observed [insert figures in Fig. 1(j) and (o)], which disappears in the monolayer WSe₂. It corresponds to the B_{2g} resonance mode of WSe₂²⁰. In general, the B_{2g} signature mode is only active in the bilayer or few-layer WSe₂, which could reflect the presence of the additional interlayer interaction in the present TMDs heterostructures²⁰. It demonstrates that the B_{2g} mode is more sensitive to interlayer interaction than the out-of-plane modes A_{1g}¹⁹⁻²¹.

Band structures for heterostructures. The conduction band minimum (CBM) and valence band maximum (VBM) at the K point are primarily composed of the Mo or W d_{z²} states, while the CBM at K-Γ and the VBM at Γ are dominated by the Mo or W d_{z²} and s p states. The Mo d_{xz,yz} states are far away from the Fermi energy¹³. Because of different orbital character, the highest valence and lowest conduction states respond very differently to the interlayer spacing and coupling. For a detailed research for the interlayer spacing and coupling, the DFT calculations for MoS₂-WS₂, MoS₂-WSe₂, and WS₂-WSe₂ heterostructures have been carried out, which are shown in Fig. 2.

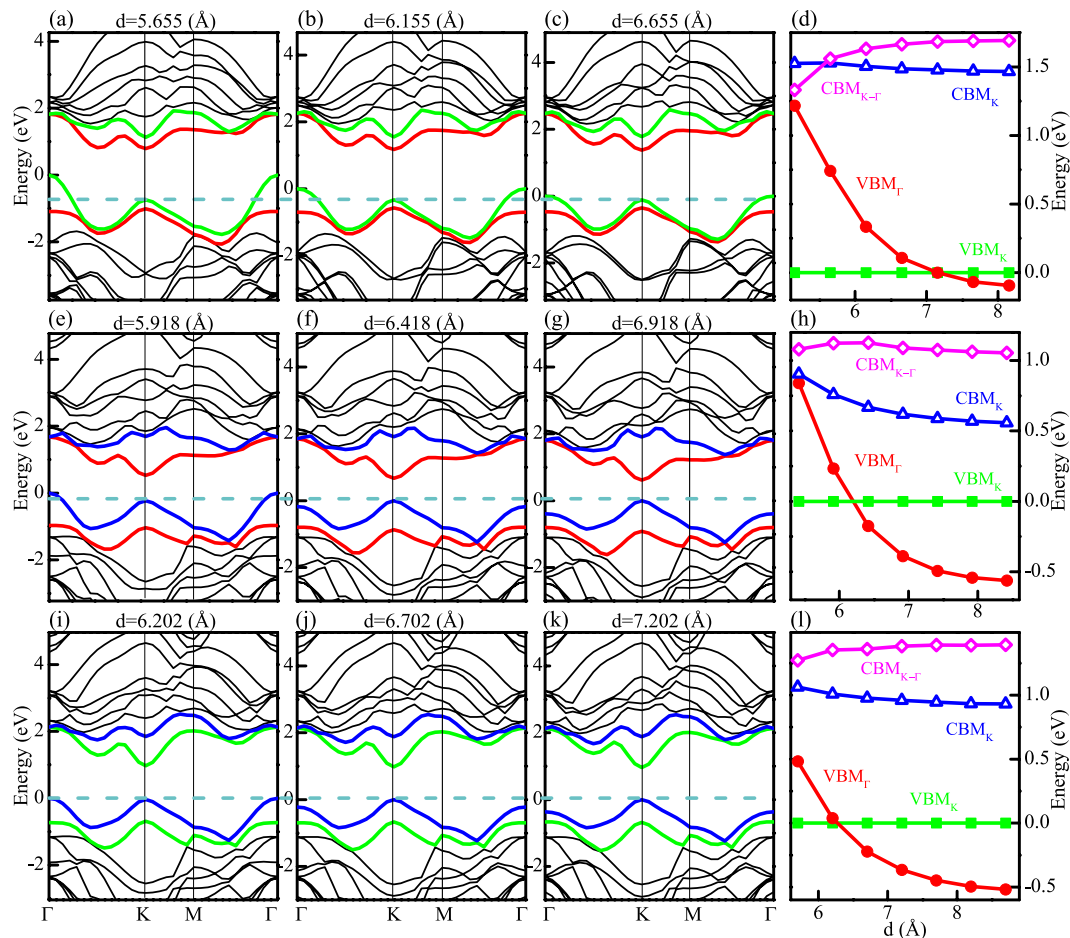


Figure 2. The band structures for $\text{MoS}_2\text{-WS}_2$, $\text{MoS}_2\text{-WSe}_2$, and $\text{WS}_2\text{-WSe}_2$ heterostructures. (a–c) Band structures for $\text{MoS}_2\text{-WS}_2$ when the layer spacing is (a) 0.5 Å smaller than the equilibrium distances, (b) equal to the equilibrium distances, (c) and 0.5 Å more than the equilibrium distances. (e–g) Band structures for $\text{MoS}_2\text{-WSe}_2$ when the layer spacing is (e) 0.5 Å smaller than the equilibrium distances, (f) equal to the equilibrium distances, and (g) 0.5 Å more than the equilibrium distances. (i–k) Band structures for $\text{WS}_2\text{-WSe}_2$ when the layer spacing is (i) 0.5 Å smaller than the equilibrium distances, (j) equal to the equilibrium distances, and (k) 0.5 Å more than the equilibrium distances. (d, h, l) Variation of the VBM and CBM with respect to the the layer spacing for (d) $\text{MoS}_2\text{-WS}_2$, (h) $\text{MoS}_2\text{-WSe}_2$, and (l) $\text{WS}_2\text{-WSe}_2$. VBM_K and CBM_K refer to the local highest valence and lowest conduction states at K point, VBM_Γ to the Γ point, and $\text{CBM}_{K-\Gamma}$ to the path K- Γ .

The equilibrium interlayer separation distances with geometry optimization for $\text{MoS}_2\text{-WS}_2$, $\text{MoS}_2\text{-WSe}_2$, and $\text{WS}_2\text{-WSe}_2$ heterostructures are 6.155 Å, 6.418 Å, and 6.702 Å, respectively. The corresponding band structures near the equilibrium layer spacing are shown in Fig. 2(a–c) ($\text{MoS}_2\text{-WS}_2$), Fig. 2(e–g) ($\text{MoS}_2\text{-WSe}_2$), and Fig. 2(i–k) ($\text{WS}_2\text{-WSe}_2$). Interestingly, at the equilibrium layer spacing of 6.155 Å in the $\text{MoS}_2\text{-WS}_2$ heterostructure, the VBM is at the Γ point because of the interaction between layers [Fig. 2(b)]. This results in an indirect transition from the VBM at the Γ point to the CBM at the K points. It is different from the direct transition situated at K point of the monolayer TMDs. The VBM at the Γ point becomes even higher to the K point when the interlayer separation distances is reduced to 5.655 Å in Fig. 2(a). The results are more obvious in Fig. 2(d), which shows the variations of the highest valence and lowest conduction states as functions of the layer spacing in $\text{MoS}_2\text{-WS}_2$. It can be seen that the reduction in the interlayer spacing modifies the VBM and CVM values at high symmetry points effectively. As the VBM at the Γ point involving p - d orbital coupling, it changes dramatically. As a result, the indirect bandgap increases obviously for shorter layer spacing. With decreasing the layer spacing from 7.155 Å to 5.155 Å, not only the VBM at Γ point becomes higher with respect to the K point, but also the CBM at a midpoint between K and Γ points becomes lower than that at the K point. However, the direct excitonic transition energy at the K point shows small changes.

The band structures for $\text{MoS}_2\text{-WSe}_2$ [Fig. 2(e–h)] and $\text{WS}_2\text{-WSe}_2$ [Fig. 2(i–l)] are quite different from for $\text{MoS}_2\text{-WS}_2$ heterostructure. The $\text{MoS}_2\text{-WSe}_2$ and $\text{WS}_2\text{-WSe}_2$ show direct gaps at the K point around 1 eV at the equilibrium layer spacing²², and the VBM at the Γ point changes less obviously than the $\text{MoS}_2\text{-WS}_2$ heterostructure. Especially for the $\text{WS}_2\text{-WSe}_2$ heterojunction, even though the interlayer separation distances is reduced 0.5 Å from the equilibrium layer spacing, the indirect transition is not as obvious as the other two heterostructures. Moreover, by varying the interlayer distance from 7.702 to 5.702 Å, the VBM at the Γ point for $\text{WS}_2\text{-WSe}_2$ changes

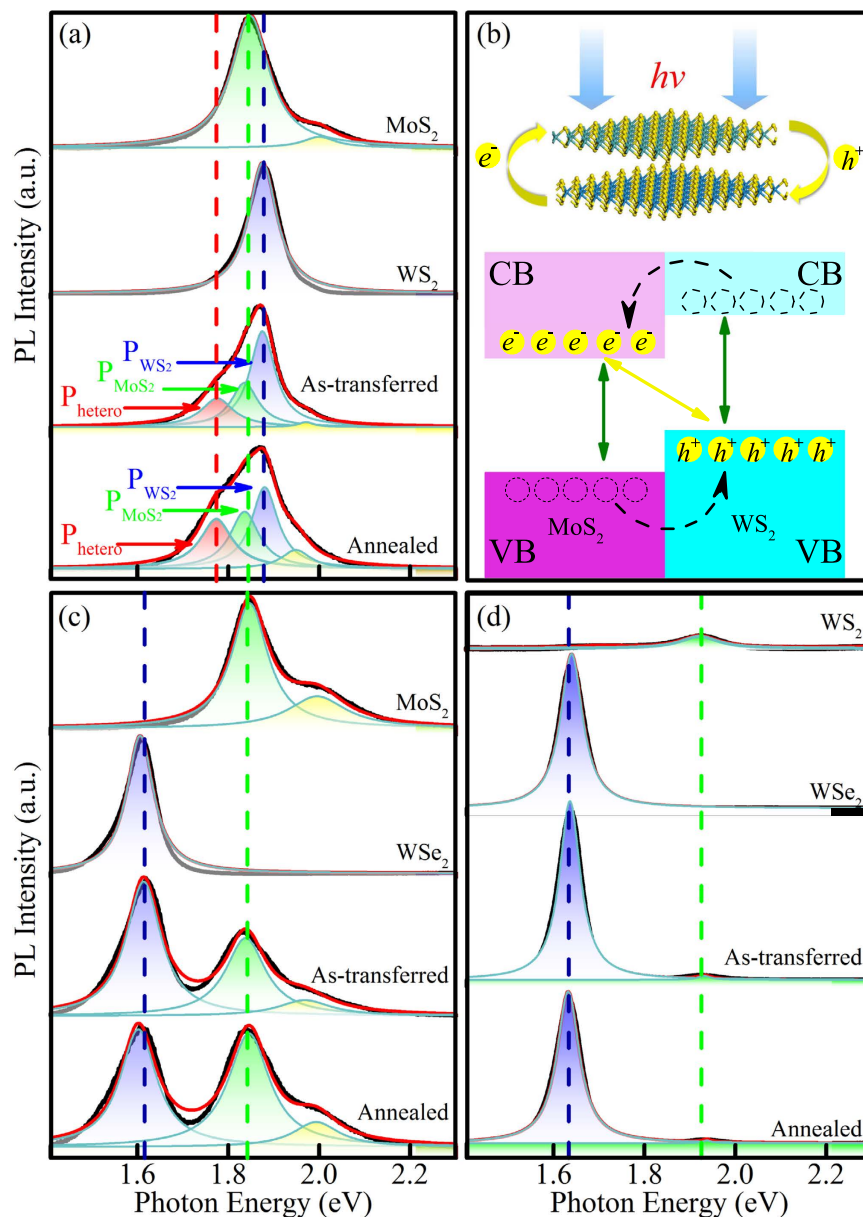


Figure 3. (a) Multiple-peak fitting to measured PL spectra of MoS₂, WS₂, as-transferred, and annealed MoS₂-WS₂ heterostructures. (b) Schematic of the band alignment at the K-point for the MoS₂-WS₂ heterostructure. (c) Multiple-peak fitting to measured PL spectra of MoS₂, WSe₂, as-transferred, and annealed MoS₂-WSe₂ heterostructures. (d) Multiple-peak fitting to measured PL spectra of WS₂, WSe₂, as-transferred, and annealed WS₂-WSe₂ heterostructures. Lorentz Model was used in the fitting to the PL spectra.

only 1 eV, which is less than those of about 1.3 eV in the MoS₂-WS₂ heterostructure. This phenomenon indicates that the interlayer coupling tuning with interlayer separation distances for WS₂-WSe₂ heterostructure is relatively difficult, which is in accordance with the presenting experimental results.

Variable-temperature tuning process. From tight-binding theory or quantum tunneling model, the interlayer interaction is expected to be exponentially sensitive to the interlayer distance. In order to further confirm the theoretical calculation and investigate the interlayer coupling with different interlayer distance, variable-temperature tuning process were performed in MoS₂-WS₂, MoS₂-WSe₂, and WS₂-WSe₂ heterostructures. It has been known that the physical properties of the heterostructures could be affected by the twist angle between the two layers as observed in graphene and graphitic materials^{23,24}. To avoid the interference of the twist angle, the whole variable-temperature experiment was carried on the same point of the heterostructure. For the purpose of obtaining information on the band properties of the heterojunctions, optical properties are characterized with PL spectroscopies in Fig. 3.

All MoS₂-WS₂, MoS₂-WSe₂, and WS₂-WSe₂ heterostructures form a type II band alignment^{22,25}. In type II heterojunctions, the CBM and VBM reside in two separate materials. Moreover, the type II band alignment and

built-in potential in the heterojunctions can facilitate the photoexcited electron-hole separation and lead to an enhanced photoswitching performance compared to that in MoS₂/WS₂ and WSe₂²⁶. For example, in MoS₂-WS₂ heterostructure, due to the type-II band alignment, photoexcited electrons and holes will relax (dashed lines in Fig. 3(b)) to the conduction band edge of MoS₂ and the valence band edge of WS₂, respectively. The coulomb attraction between electrons in MoS₂ and holes in WS₂ gives rise to an interlayer exciton P_{hetero} . It is analogous to spatially indirect excitons in coupled quantum wells²⁷. Therefore, a new peak at 1.77 eV is observed [P_{hetero} in Fig. 3(a)], lying interestingly at a lower energy than the peak for the two constituent single layers. It is noteworthy that the relative intensity for P_{hetero} and MoS₂, WS₂ changed after the annealing progress. The relative intensity of P_{hetero} to P_{MoS_2} is expressed as $I_{h/Mo}$, P_{hetero} to P_{WS_2} is $I_{h/W}$. After the annealing progress, $I_{h/Mo}$ increases from 0.65 to 0.87, $I_{h/W}$ increases from 0.3 to 0.61. Such a pronounced luminescence effect in the heterostructure suggests that most electrons excited in WS₂ transfer to the lower states in MoS₂, instead of forming excitons in WS₂ and recombine radiatively. The annealing progress promote the electrons transfer in the heterostructure, as the annealing is able to drive out trapped residual molecules²⁸. However, in equilibrium condition of the MoS₂-WSe₂ and WS₂-WSe₂ heterostructures, the direct gaps at the K point are around 1 eV [Fig. 2(f) and (j)], which are different from the indirect transition of MoS₂-WS₂²². Under these conditions, the PL spectra from 1.4 eV to 2.3 eV for MoS₂-WSe₂ and WS₂-WSe₂ heterostructures in Fig. 3(c) and (d) appear to comprise the addition of the constituent layers.

In the variable-temperature tuning process for the MoS₂-WS₂, the excitonic transitions of MoS₂ (P_{MoS_2}), WS₂ (P_{WS_2}), and interlayer exciton (P_{hetero}) are fitted with the integrated intensity peak P_M , with the purpose of describing the intensity change with temperature. Figure 4(a) shows the luminescence evolutions of the MoS₂-WS₂ heterostructure as a function of temperature from 77 to 275 K with a stability of about 0.1 K. When the excitonic transitions of MoS₂ (P_{MoS_2}), WS₂ (P_{WS_2}), and interlayer exciton (P_{hetero}) are fitted with the integrated intensity peak P_M , the PL spectra can be deconvoluted into three major peaks when the temperature is below 225 K. The resonance at about 2 eV corresponds to the B exciton, which attributes to the top of valence-band splitting due to the strong spin-orbital interaction in MoS₂²⁹. In addition to the above excitons, another transition at a lower energy can be observed at about 1.7 eV, which seems different from the previous work^{30,31}. The transition becomes negligible in the temperature above 250 K [$P_{indirect}$ in Fig. 4(a),(d) and (g)]. This characteristic is profoundly different from the behaviors of other double layer transition metal sulfides. Nanostructures obtained from indirect bandgap transition metal sulfides emit an indirect transition excitons upon photoexcitation, but the luminescence is present in the room temperature as well (Figure S1)³². In order to identify the peak $P_{indirect}$, another significant change should be noticed. When the temperature increases above 250 K, the intensity of the peak P_M increases dramatically by about three times. The integral PL intensity generally decreases with increasing the temperature. The phenomena can be observed in temperature dependent PL measurement of monolayer MoS₂, as shown in Figure S2. This quenching effect is due to that the nonradiative electron-hole recombination rate increases exponentially with increasing the temperature^{33,34}. The nonradiative channels, such as trapping by surface/defect/ionized impurity states, become thermally activated with increasing the temperature and the nonradiative lifetime τ_{NR} is expressed as ref. 35

$$\tau_{NR} = \tau_0 \exp\left(\frac{E_a}{k_B T}\right) \quad (1)$$

where τ_0 is the pre-exponential factor, E_a is the activation energy in the thermal quenching process and k_B is the Boltzmann constant. When the temperature increases, the decreasing τ_{NR} results in a decrease in the luminescence intensity, which can be expressed as ref. 36

$$I = \frac{I_0}{1 + A \exp\left(-\frac{E_a}{k_B T}\right)} \quad (2)$$

where I_0 is the intensity at 0 K, A is a parameter related to radiative lifetime (τ_R) as $A = \tau_R/\tau_0$, and τ_R is the radiative lifetime. However, the peak P_M reveals the monotonic decrease of PL intensity with increasing the temperature only when the temperature is below 250 K, and the PL intensity is even stronger when the temperature is above 250 K in spite of the increasing temperature.

In order to explain the extraordinary change of the P_M intensity, the luminescence quantum efficiency is introduced. As the luminescence physics mechanism for transition metal sulfide is different from traditional silicon nanocrystals. In silicon nanocrystals, the photoluminescence originates from quantum confined electronic states with increased emission energy at decreased nanoparticle size. The radiative transition rate is quite low. In contrast, luminescence for transition metal sulfide arises from electronic transitions, which shows a much higher radiative recombination rate. Therefore, the extraordinary change of the P_M intensity is explained by luminescence quantum efficiency, which is approximated by ref. 37

$$\eta_{lum} = \frac{k_{rad}}{k_{rad} + k_{relax} + k_{defect}} \quad (3)$$

where k_{rad} is the rates of radiative recombination, k_{relax} is electron relaxation within the conduction and valence bands, and k_{defect} is defect trapping, respectively. The k_{rad} is not likely to change appreciably with the change of the interlayer spacing in heterostructure, because the direct excitonic transitions at Γ point do not show significant change. The k_{defect} is stable relatively. Therefore, when the temperature increases above 250 K, the significant

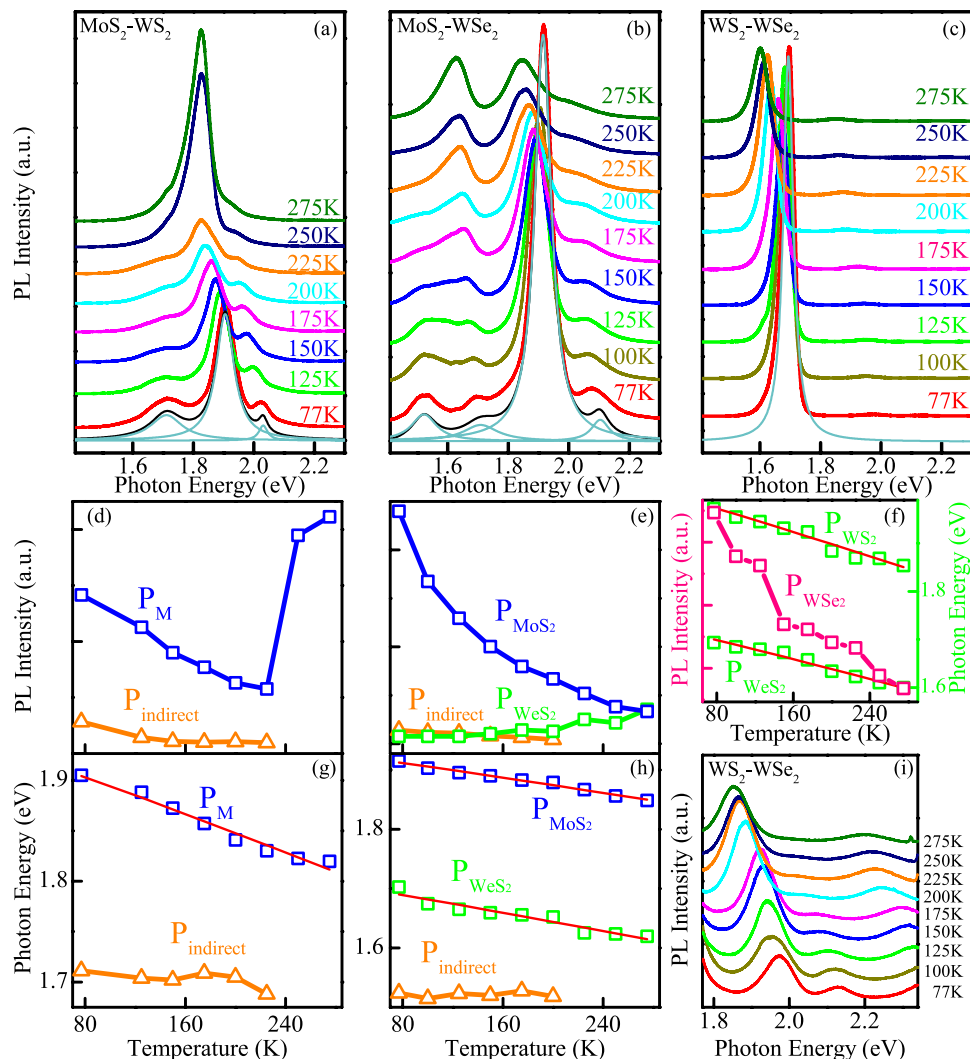


Figure 4. Temperature dependent PL of heterostructures (a) $\text{MoS}_2\text{-WS}_2$, (b) $\text{MoS}_2\text{-WSe}_2$, (c) and $\text{WS}_2\text{-WSe}_2$. In the bottom of the spectra (a), (b), and (c), the Lorentzian fit functions to the spectra are shown. (d) Fitted PL intensity and (g) peak position of the direct transition integrated intensity P_M and indirect transition P_{indirect} versus temperature in $\text{MoS}_2\text{-WS}_2$ heterostructure. (e) Fitted PL intensity and (h) peak position of the P_{MoS_2} , P_{WSe_2} , and P_{indirect} in $\text{MoS}_2\text{-WSe}_2$ heterostructure. (f) Fitted PL Peak position and intensity of the P_{WSe_2} in $\text{WS}_2\text{-WSe}_2$ heterostructure. (i) Enhanced temperature dependent PL spectra of $\text{WS}_2\text{-WSe}_2$ heterostructure between 1.77 eV and 2.34 eV.

enhanced luminescence of P_M has to be attributed to the dramatically reduced electronic relaxation k_{relax} . The decrease of interband relaxation rate strongly suggests a substantial change in the $\text{MoS}_2\text{-WS}_2$ heterostructure electronic structure when the temperature increases from 225 K to 250 K. It is noteworthy that the value of the phonon-assisted k_{relax} is very large for the indirect bandgap semiconductor. Because when the indirect bandgap disappears, the decay rate via phonons decreases enormously^{32,37}. As a consequence, when the temperature increases from 225 K to 250 K, the indirect bandgap disappears. The substantial change is in accordance with the transition transformation analysed in the DFT calculations. The indirect transition from the VBM at Γ point to the CBM at K point disappeared with increasing the interlayer spacing. Based on the above analysis, the transition P_{indirect} disappeared above 250 K is attributed to indirect band gap emission.

It is noteworthy that, the $\text{MoS}_2\text{-WSe}_2$ prefers direct transition at the equilibrium layer spacing, and the VBM at the Γ point for the $\text{MoS}_2\text{-WSe}_2$ band structure changes less obviously than the $\text{MoS}_2\text{-WS}_2$ [Fig. 2(e–h)]. In the luminescence evolutions of $\text{MoS}_2\text{-WSe}_2$ heterostructure [Fig. 4(b)], another indirect transition peak P_{indirect} emerges at the temperature below 225 K [Fig. 4(e)]. However, the luminescence trends for the P_{MoS_2} and P_{WSe_2} are different from $\text{MoS}_2\text{-WS}_2$. Among the heterostructures studied, the atomic differences in $\text{MoS}_2\text{-WSe}_2$ are the most obvious. Both the transition metals and the sulfur family elements are different. As a consequence, the WSe_2 attributed part in the band structure is significantly influenced in the heterostructure [blue line in Fig. 2(f)]. An indirect transition from the VBM of WSe_2 to the WSe_2 induced conduction band between Γ and K points is caused. Moreover, the P_{indirect} is quenching with increasing the temperature [Fig. 4(b) and e)], as the influence in the

Samples	exciton	E_0 (eV)	S	$\langle \hbar\omega \rangle$ (meV)
MoS ₂ -WS ₂	P_M	1.92	2.78	9.60
MoS ₂ -WSe ₂	P_{MoS_2}	1.93	1.91	8.63
	P_{WSe_2}	1.71	2.23	6.42
WS ₂ -WSe ₂	P_{WS_2}	2.00	3.72	7.84
	P_{WSe_2}	1.72	2.99	6.11

Table 1. Fitting parameters of the PL peak energy as a function of temperature extracted in Fig. 4(f–h).

band structure of the WSe₂ attributed part declines when the interlayer spacing increases. Along with the quenching of the indirect transition, the direct transition excitons increase, and the P_{WSe_2} increases gradually. However, the VBM at the Γ point in the MoS₂-WSe₂ heterostructure is less sensitive to the interlayer spacing than the MoS₂-WS₂ heterostructure [Fig. 2]. Therefore, the dramatically increasing intensity of the PL has not been observed here.

Not only for MoS₂-WSe₂, but the VBM at the Γ point for WS₂-WSe₂ heterostructure is insensitive to the interlayer spacing [Fig. 2(l)]. Moreover, the indirect transition for WSe₂ in the WS₂-WSe₂ is less obvious than that in the MoS₂-WSe₂ heterostructure. As a consequence, the P_{WS_2} and P_{WSe_2} present a redshift for conventional semiconductor. In addition, it is important to note that the B exciton peak of WS₂ and WSe₂ can be observed in the enhanced PL spectra of WS₂-WSe₂ heterostructure in Fig. 4(i). The peaks near 1.98 eV and above 2.3 eV at 77 K are attributed to be the A and B exciton of WS₂^{17,32}. The peak near 2.13 eV at 77 K corresponds to the B exciton of WSe₂. It is 430 meV higher than the A exciton, which is in agreement with the previous reports³². The B exciton peak for WS₂ and WSe₂ with such an intensity is rarely observed in the previous PL measurement. What is more, it is discovered for the first time that the B exciton peak for WSe₂ quenches with increasing the temperature.

Along with changing of the luminescent intensity, the direct transition in the heterostructures experiences a large redshift with increasing the temperature, as shown in Fig. 4(f–h). Such behavior is similar to the response of conventional semiconductors under high temperature, which result from the increased electron-phonon interactions and slight changes in bonding lengths. Thus, it provides a method to evaluate temperature of the semiconductor^{38,39}. By employing a modified Varshni relationship, the temperature dependence of the PL peak position is fitted using^{40,41}

$$E(T) = E_0 - S \langle \hbar\omega \rangle \left[\coth \frac{\langle \hbar\omega \rangle}{2k_B T} - 1 \right]. \quad (4)$$

where E_0 is the emission energy at zero absolute temperature, S is the Huang-Rhys factor that represents the coupling strength of exciton-phonon, $\langle \hbar\omega \rangle$ is the average phonon energy, \hbar and k_B are the Planck and Boltzmann constant, respectively. As shown in Fig. 4(f–h), the fitting parameters are extracted. Table 1 lists the fitting values of E_0 , S , and $\langle \hbar\omega \rangle$ for MoS₂, WS₂, and WSe₂ in the heterostructures. By comparing these parameters, especially S , between the TMD in the heterostructures and monolayer^{38,42}, the contribution of the interlayer coupling can be informed. Moreover, with the help of this expression, it is possible to derive the temperature difference of the above heterostructure in the device where the PL is measured by comparing the emission energy difference^{38,43}. However, from Fig. 4(g,h), the peak $P_{indirect}$ do not show an obvious redshift as the P_M , P_{MoS_2} , or P_{WSe_2} , which is due to the gradual decreasing VBM at the Γ point caused by increasing the interlayer spacing with the temperature. As shown in Figure S1, this decrease of VBN at the Γ point results in a blueshift of the indirect transition in double layer WS₂.

Conclusions

To summarize, the interlayer coupling tuning of 2D heterostructures formed with CVD-grown monolayer MoS₂, WS₂, and WSe₂ is carried out by thermal annealing process and variable-temperature experiment. By comparing the tuning methods, the conclusion is made that the temperature is an extremely sensitive factor to the interlayer coupling. Based on the DFT calculations, an interesting phenomenon is found that MoS₂-WS₂, MoS₂-WSe₂, and WS₂-WSe₂ heterostructures turn into direct-gap semiconductors from indirect-gap semiconductors with increasing the interlayer space. Furthermore in the MoS₂-WS₂, MoS₂-WSe₂, and WS₂-WSe₂ heterostructures, the electronic structure changing process with interlayer spacing is different from each other. Our results highlight the significance of interlayer coupling in tuning the light emission of TMDs and offer a general route to prepare large-area TMD tandem structures for fundamental study as well as electronic and photovoltaic applications.

Methods

Synthesis of MoS₂, WS₂ and WSe₂. The MoS₂ monolayers were grown by low-pressure CVD technique for 10 min. The SiO₂/Si substrates were cleaned using piranha solution (a volumetric mixture of 3:1 of 98% H₂SO₄ to 35% H₂O₂), then placed in the center of the quartz tube's heating zone and heated to 850 °C in argon atmosphere to restrict further oxidation. The molybdenum trioxide (MoO₃) powder was loaded in front of the substrates, while the sulfur powder was placed in the front of the quartz tube, which was heated to 200 °C by a heating band as shown in Figure S3. The WS₂ and WSe₂ monolayers were separately fabricated by constant-pressure vapor phase deposition method at 1100 °C and 1200 °C in argon atmosphere for 10 min.

Transfer Method. The TMDs obtained by mechanical exfoliation have a small flake size, and it is not possible to create large scale heterostructured materials. Thus, the heterostructures here were prepared from chemical vapor deposition (CVD) growth (see Supporting Information Figure S3).

Figure S4 illustrates the polystyrene (PS) film transfer technique schematically. The process started by coating a layer of polymer on top of the as-grown TMDs. The polymer acted as carrier layer, which can help with the handling of the atomically thin materials. The 10 wt% PS was dissolved in toluene. It was spin-coated on the CVD grown monolayer TMDs/SiO₂/Si with a speed of 3500 rpm for 1 minute. Then, the samples with coating layer were baked at 90 °C for 1 hour. This was designed to evaporate the toluene and eliminate air bubbles formed at the interface of monolayer TMDs and PS, so that the adhesion is increased. This was followed by a gentle poking made by a glass cutter at the edge of the PS/TMDs/SiO₂/Si to expose SiO₂, by this way, the water penetration in the next step can be improved. Then, the PS/TMDs/SiO₂/Si was sank into a large drop of deionized water in the hydrophobic plastic petri dishes gently. This water penetration operation was repeated for several times, until the PS/TMDs film was floated on the top of the water because of the repulsion between the PS and water. Next, the substrate was taken away, and another TMDs/SiO₂/Si was put into the water from the side. After that, the system was dried by simply sucking the water droplet away with a paper towel. During this process, the PS/TMDs was fixed above the TMDs/SiO₂/Si with a tweezers. After the PS/TMDs was transferred to the TMDs/SiO₂/Si, the bubbles in the transferred assembly were purged out with the hydrogen. In order to combine the heterostructures better, the samples were baked at 90 °C for 30 min to remove water residues, and then at 120 °C for 30 min to spread the polymer for the elimination of possible wrinkles. Finally, the transferred assembly was soaked in toluene for at least 2 hours with the toluene changed several times during this time. It was worth noting that the obtained heterostructures were much cleaner than the conventional polymethyl methacrylate (PMMA) transfer techniques with reduced transfer film residue and improved quality (Figure S5)^{44,45}. Besides, the new transfer technique has the advantage of high efficiency on account of the regardless of the thickness of spin-coating layer.

Raman/PL Spectroscopy. Temperature dependent PL experiments were carried out by a Jobin-Yvon LabRAM HR 800 micro-Raman spectrometer and a THMSE 600 heating/cooling stage (Linkam Scientific Instruments) in the temperature range from −196 °C to 2 °C with a resolution of 0.1 °C. The heterostructures was excited by the 488 nm line of an Ar laser with the output power of 20 mW and recorded in back-scattering geometry with a resolution of better than 1 cm^{−1}. The laser beam was focused through a 50× microscope with a working distance of 18 mm. An air-cooled CCD (−70 °C) with a 1024 × 256 pixels front illuminated chip was used to collect the scattered signal dispersed on 1800 grooves/mm grating for Raman and 600 grooves/mm grating for PL⁴⁶. Peaks of the bare spectra are assigned by using the supporting software NGS LabSpec designed by Jobin Yvon.

Computational Details. Our density functional theory (DFT) calculations were performed with plane-wave pseudopotentials from the calculate method of quantum mechanics^{47,48}. The generalized gradient approximation (GGA) for exchange-correlation term was employed, and the functional was adopted for structure optimization and band gaps calculation⁴⁹. The selected pseudopotential is Ultrasoft Pseudopotentials. To acquire accurate results for bilayer structures, DFT-D approach was included with the Ortmann–Bechstedt–Schmidt (OBS) vdW correction⁵⁰, which gives the structural parameters in good agreement with experimental values. A planewave cutoff energy of 320 eV and a 5 × 5 × 1 grid of Monkhorst-Pack points were employed to ensure good convergence of the computed structures and energies. Geometry optimization was determined using the Broyden–Fletcher–Goldfarb–Shenno (BFGS) minimization technique, with thresholds of converged structure of energy change per atom smaller than 10^{−5} eV/atom, and displacement of atoms during geometry optimization no more than 0.001 Å. The tolerance in the self-consistent field (SCF) calculation was 1.0 × 10^{−6} eV/atom. All calculations were carried out using a 1 × 1 supercell with vacuum thickness not smaller than 17 Å and spin-orbit coupling was not included.

References

- Geim, A. K. & Grigorieva, I. V. Van der Waals Heterostructures. *Nature* **499**, 419–425 (2013).
- Mak, K. F., Lee, C., Hone, J., Shan, J. & Heinz, T. E. Atomically Thin MoS₂: A New Direct-Gap Semiconductor. *Phys. Rev. Lett.* **105**, 136805 (2010).
- Wang, Q. H., Kalantar-Zadeh, K., Kis, A., Coleman, J. N. & Strano, M. S. Electronics and Optoelectronics of Two-Dimensional Transition Metal Dichalcogenides. *Nat. Nanotechnol.* **7**, 699–712 (2012).
- Yu, T. & Wu, M. W. Valley Depolarization Dynamics and Valley Hall Effect of Excitons in Monolayer and Bilayer MoS₂. *Phys. Rev. B* **93**, 045414 (2016).
- Midya, A., Ghorai, A., Mukherjee, S., Maiti, R. & Ray, S. K. Hydrothermal Growth of Few Layer 2H-MoS₂ for Heterojunction Photodetector and Visible Light Induced Photocatalytic Applications. *J. Mater. Chem. A* **4**, 4534–4543 (2016).
- Shih, C.-K. Coherently Strained in-Plane Atomic Layer Heterojunctions. *NPG Asia Mater.* **7**, e231 (2015).
- Huang, C. *et al.* Lateral Heterojunctions within Monolayer MoSe₂-WSe₂ Semiconductors. *Nat. Mater.* **13**, 1096–1101 (2014).
- Li, D. *et al.* Multimodal Nonlinear Optical Imaging of MoS₂ and MoS₂-Based van der Waals Heterostructures. *ACS Nano* **10**, 3766–3775 (2016).
- Huo, N. *et al.* Novel Optical and Electrical Transport Properties in Atomically Thin WSe₂/MoS₂ p-n Heterostructures. *Adv. Electron. Mater.* **1**, 1400066 (2015).
- Hong, T. *et al.* Anisotropic Photocurrent Response at Black Phosphorus-MoS₂ p-n Heterojunctions. *Nanoscale* **7**, 18537–18541 (2015).
- Kosmider, K. & Fernández-Rossier, J. Electronic Properties of the MoS₂-WS₂ Heterojunction. *Phys. Rev. B* **87**, 075451 (2013).
- Rivera, P. *et al.* Observation of Long-Lived Interlayer Excitons in Monolayer MoSe₂-WSe₂ Heterostructures. *Nat. Commun.* **6**, 6242 (2015).
- Tongay, S. *et al.* Tuning Interlayer Coupling in Large-Area Heterostructures with CVD-Grown MoS₂ and WS₂ Monolayers. *Nano Lett.* **14**, 3185–3190 (2014).
- Steward, E. G., Cook, B. P. & Kellett, E. A. Dependence on Temperature of the Interlayer Spacing in Carbons of Different Graphitic Perfection. *Nat.* **187**, 1015–1016 (1960).

15. Walker, P. L., McKinstry, H. A. & Wright, C. C. X-Ray Diffraction Studies of a Graphitized Carbon - Changes in Interlayer Spacing and Binding Energy with Temperature. *Industrial and Engineering Chemistry, Ind. Eng. Chem.* **45**, 1711–1715 (1953).
16. Yan, R. *et al.* Thermal Conductivity of Monolayer Molybdenum Disulfide Obtained from Temperature-Dependent Raman Spectroscopy. *ACS Nano* **8**, 986–993 (2014).
17. Gutiérrez, H. R. *et al.* Extraordinary Room-Temperature Photoluminescence in Triangular WS₂ Monolayers. *Nano Lett.* **13**, 3447–3454 (2013).
18. Terrones, H. *et al.* New First Order Raman-active Modes in Few Layered Transition Metal Dichalcogenides. *Sci. Rep.* **4**, 4215 (2014).
19. Luo, X. *et al.* Effects of Lower Symmetry and Dimensionality on Raman Spectra in Two-Dimensional Wse₂. *Phys. Rev. B* **88**, 195313 (2013).
20. Zhou, H. *et al.* Large Area Growth and Electrical Properties of *p*-Type Wse₂ Atomic Layers. *Nano Lett.* **15**, 709–713 (2015).
21. Li, H. *et al.* Mechanical Exfoliation and Characterization of Single- and Few-Layer Nanosheets of Wse₂, TaS₂, and TaSe₂. *Small* **9**, 1974–1981 (2013).
22. Terrones, H., López-Uras, F. & Terrones, M. Novel Hetero-Layered Materials with Tunable Direct Band Gaps by Sandwiching Different Metal Disulfides and Diselenides. *Sci. Rep.* **3**, 1549 (2013).
23. Kim, Y. *et al.* Charge Inversion and Topological Phase Transition at a Twist Angle Induced van Hove Singularity of Bilayer Graphene. *Nano Lett.* **16**, 5053–5059 (2016).
24. Yan, W. *et al.* Angle-Dependent van Hove Singularities in a Slightly Twisted Graphene Bilayer. *Phys. Rev. Lett.* **109**, 126801 (2012).
25. Kang, J., Tongay, S., Zhou, J., Li, J. & Wu, J. Band Offsets and Heterostructures of Two-Dimensional Semiconductors. *Appl. Phys. Lett.* **102**, 012111 (2013).
26. Huo, N. *et al.* Tunable Polarity Behavior and Self-Driven Photoswitching in *p*-Wse₂/*n*-WS₂ Heterojunctions. *Small* **11**, 5430–5438 (2015).
27. Fang, H. *et al.* Strong Interlayer Coupling in van der Waals Heterostructures Built from Single-Layer Chalcogenides. *Natl. Acad. Sci. USA* **111**, 6198–6202 (2014).
28. Coy Diaz, H., Addou, R. & Batzill, M. Interface properties of CVD grown graphene transferred onto MoS₂(0001). *Nanoscale* **6**, 1071–1078 (2014).
29. Mouri, S., Miyauchi, Y. & Matsuda, K. Tunable Photoluminescence of Monolayer MoS₂ via Chemical Doping. *Nano Lett.* **13**, 5944–5948 (2013).
30. Gong, Y. *et al.* Vertical and in-plane heterostructures from WS₂/MoS₂ monolayers. *Nat. Mater.* **13**, 1135–1142 (2014).
31. Kozawa, D. *et al.* Evidence for Fast Interlayer Energy Transfer in MoSe₂/WS₂ Heterostructures. *Nano Lett.* **16**, 4087–4093 (2016).
32. Zhao, W. *et al.* Evolution of Electronic Structure in Atomically Thin Sheets of WS₂ and Wse₂. *ACS Nano* **7**, 791–797 (2013).
33. Schubert, E., Gessmann, T. & Kim, J. *Light Emitting Diodes*; Cambridge University Press: Cambridge, UK (2006).
34. Ji, C. *et al.* Temperature-Dependent Photoluminescence of Ag₂Se Quantum Dots. *J. Phys. Chem. C* **119**, 13841–13846 (2015).
35. Makino, T. *et al.* Temperature Quenching of Exciton Luminescence Intensity in ZnO/(Mg, Zn)O Multiple Quantum Wells. *J. Appl. Phys.* **93**, 5929–5933 (2003).
36. Fonoberov, V. A., Alim, K. A., Balandin, A. A., Xiu, F. & Liu, J. Photoluminescence Investigation of the Carrier Recombination Processes in ZnO Quantum Dots and Nanocrystals. *Phys. Rev. B* **73**, 165317 (2006).
37. Splendiani, A. *et al.* Emerging Photoluminescence in Monolayer MoS₂. *Nano Lett.* **10**, 1271–1275 (2010).
38. He, Z. *et al.* Layer-Dependent Modulation of Tungsten Disulfide Photoluminescence by Lateral Electric Fields. *ACS Nano* **9**, 2740–2748 (2015).
39. König, U. L. F. & Langmann, U. Temperature Distribution in Gunn Diodes and GaAs MESFETs Determined by Micro-photoluminescence. *Trans. Electron Devices* **25**, 49–55 (2013).
40. Varshni, Y. P. Temperature Dependence of the Energy Gap in Semiconductors. *Physica* **34**, 149–154 (1967).
41. Mitoglu, A. A. *et al.* Optical manipulation of the exciton charge state in single-layer tungsten disulfide. *Phys. Rev. B* **88**, 245403 (2013).
42. Tongay, S. *et al.* Thermally Driven Crossover from Indirect toward Direct Bandgap in 2D Semiconductors: MoSe₂ versus MoS₂. *Nano Lett.* **12**, 5576–5580 (2012).
43. König, U. & Langmann, U. Temperature Distribution in Gunn Diodes and GaAs MESFET's Determined by Micro-Photoluminescence. *Trans. Electron Devices* **25**, 49–55 (1978).
44. Gurarlan, A. *et al.* Surface-Energy-Assisted Perfect Transfer of Centimeter-Scale Monolayer and Few-Layer MoS₂ Films onto Arbitrary Substrates. *ACS Nano* **8**, 11522–11528 (2014).
45. Xu, Z.-Q. *et al.* Synthesis and Transfer of Large-Area Monolayer WS₂ Crystals: Moving Toward the Recyclable Use of Sapphire Substrates. *ACS Nano* **9**, 6178–6187 (2015).
46. Huang, T. *et al.* Inherent Optical Behavior and Structural Variation in Na_{0.5}Bi_{0.5}TiO₃–6% BaTiO₃ Revealed by Temperature Dependent Raman Scattering and Ultraviolet-Visible Transmittance. *Appl. Phys. Lett.* **104**, 111908 (2014).
47. Hohenberg, P. & Kohn, W. Inhomogeneous Electron Gas. *Phys. Rev.* **136**, B864–B871 (1964).
48. Kohn, W. & Sham, L. J. Quantum Density Oscillations in an Inhomogeneous Electron Gas. *Phys. Rev.* **137**, A1697–A1705 (1965).
49. Perdew, J. P. & Wang, Y. Accurate and Simple Analytic Representation of the Electron-Gas Correlation Energy. *Phys. Rev. B* **45**, 13244–13249 (1992).
50. Ortman, F., Bechstedt, F. & Schmidt, W. G. Semiempirical van der Waals Correction to the Density Functional Description of Solids and Molecular Structures. *Phys. Rev. B* **73**, 205101 (2006).

Acknowledgements

This work was financially supported by Major State Basic Research Development Program of China (Grant No. 2013CB922300), Natural Science Foundation of China (Grant Nos 11374097, 61376129, 61504156, and 61227902), Projects of Science and Technology Commission of Shanghai Municipality (Grant Nos 15JC1401600 and 14XD1401500), and the Program for Professor of Special Appointment (Eastern Scholar) at Shanghai Institutions of Higher Learning.

Author Contributions

F.W., Z.H. and J.Z. analyzed data and prepared the manuscript and figures. F.W. and S.G. performed experiments. J.W. and F.W. performed the first-principles calculation. The project was initiated and conceptualized by Z.H. and J.C. All authors reviewed the manuscript.

Additional Information

Supplementary information accompanies this paper at <http://www.nature.com/srep>

Competing Interests: The authors declare no competing financial interests.

How to cite this article: Wang, F. *et al.* Tuning Coupling Behavior of Stacked Heterostructures Based on MoS₂, WS₂, and WSe₂. *Sci. Rep.* 7, 44712; doi: 10.1038/srep44712 (2017).

Publisher's note: Springer Nature remains neutral with regard to jurisdictional claims in published maps and institutional affiliations.



This work is licensed under a Creative Commons Attribution 4.0 International License. The images or other third party material in this article are included in the article's Creative Commons license, unless indicated otherwise in the credit line; if the material is not included under the Creative Commons license, users will need to obtain permission from the license holder to reproduce the material. To view a copy of this license, visit <http://creativecommons.org/licenses/by/4.0/>

© The Author(s) 2017